Journal of Engineering Science and Technology
Vol. 15, No. 2 (2020) 1056 - 1078

NUMERICAL STUDY OF LEE WAVES CHARACTERISTICS IN THE OCEAN

SYAMSUL RIZAL[1,2,*], REZA WAFDAN[1], YUDI HADITIAR[2], MARWAN RAMLI[3,4], VERA HALFIANI[3,4]

[1]Marine Sciences Department, Universitas Syiah Kuala, Banda Aceh, 23111, Indonesia,
[2]Graduate School of Mathematics and Applied Sciences, Universitas Syiah Kuala, Banda Aceh, 23111, Indonesia,
[3]Department of Mathematics, Universitas Syiah Kuala, Banda Aceh, 23111, Indonesia,
[4]Dynamic Application and Optimization Research Group, Universitas Syiah Kuala, Banda Aceh, 23111, Indonesia
*Corresponding Author Email: syamsul.rizal@unsyiah.net

Abstract

This study discusses the characteristics of lee waves in a vertical ocean slice model. To analyse the characteristics, this study applies two different scenarios; the first scenario employs a vertical ocean slice model with a uniform depth of 100 m and a width of 500 m and the second scenario uses the same model but considering an undersea mountain having a width of 100 m and a height of 40 m. Simulations on motions of the waves are generated by using a numerical method. Both scenarios implement the same force, which is the sea level gradient force that is maintained until the end of simulation time. In order to observe the significance of Courant-Friedrichs-Lewy (CFL) condition, numerical experiments are conducted using two values of time step sizes, Δt = 0.1 second, which is obtained based on the CFL and Δt = 1 second, which is chosen outside the interval of CFL criterion. The results of the experiments show that applying different values of the time step sizes do not significantly affect the resulting waves for the first scenario while it gives different outputs for the second scenario. The results in the first scenario present that the currents move horizontally and their velocities speed up over time while the values of water densities do not change throughout the simulation time. In the second scenario, the horizontal and vertical currents continuously change causing disturbances to the densities. From Fast Fourier Transform analysis, it is obtained that at depths of the surface level to 60 m, the magnitudes of carrier waves in the second scenario is greater than the magnitude of the first scenario, while at depths of below 60 m, the magnitude of carrier waves from the first scenario is greater than the magnitude of the second scenario.

Keywords: Current, Density, Fast Fourier transform, Lee waves, Nonhydrostatic model.

1. Introduction

Mountain waves or lee waves are atmospheric internal gravity waves, which occur above mountains. The existence of the waves was discovered in 1933 by German glider pilots. Winds that push air parcels into obstacles like mountains deflect upward in a stably stratified atmosphere. The moving winds then return to its initial height to form up-down oscillating movements [1]. Sometimes, Mountain waves appear in cloud formations. Large-amplitude mountain waves can produce clear-air-turbulence, which poses a great danger to flights. Large-amplitude mountain waves can also generate very strong winds [2].

In ocean interior, when stably stratified water rises, a buoyancy perturbation occurs on undersea mountains. The perturbations often trigger density changes which, are conveyed to locations far from the mountains. These changes form waves known as gravity (or buoyancy) waves. Gravity waves triggered by the flows above the mountains are called mountain waves of lee waves.

A trapped nonlinear lee wave can grow up to 200 m wide and span a few kilometres away from the mountains during strong off-ridge flow [3, 4]. Due to this phenomenon, the presence of lee waves may be seriously dangerous to air traffics and undersea operations [4, 5].

Lee waves potentially propagate over large horizontal distances as well as in vertical direction through columns to a height far above the lower boundary layer. This process allows the waves to store energy for mixing in locations far from the bottom topographic features [6]. This event has crucial implications because the vertical distribution of the mixing strongly influences the simulated general circulation [7].

In contrast to the waves on the sea-surface, lee waves are not directly visible to the eye. In the deep oceans, lee waves are generated in stratified fluid through an interaction of deep geostrophic currents and undersea mountains or sills [8, 9]. Lee waves have a frequency between local inertial frequency and buoyancy frequency, which can be formed in strong bottom flow region and supercritical mount flank (the internal tidal wave slope is smaller compared to the bottom slope) [9, 10]. It was reported that in the region of supercritical mount flank of the tropical Indian Ocean, the vertical wavelength reached up to 30 meters [10].

Garabato et al. [8] mentioned that through wave drag, momentum and vorticity from the geostrophic flows are extracted by lee waves. When lee waves, which are caused by shear or convective instabilities break, energy, which is converted from geostrophic motions into lee waves dissipates [8, 11, 12].

Topographic internal lee wave and quadratic bottom boundary layer drag produce most of the dissipated energy in oceans. The dissipated energy may dissipate due to the effects of abyssal currents and stratification. According to Trossman et al. [12, 13], in a mixed layer, the energy dissipation is closely related to vertical viscosity.

The strong lee wave generation can be seen on the main sill of the Strait of Gibraltar (Caraminal Sill) [14, 15] and in the Southern Ocean [16, 17]. When lee waves of Caraminal Sill have been developed, the amplitudes of the internal waves are relatively high and chaotic [14]. The internal lee wave formation, radiation, and breaking are believed to contribute to the oceanic momentum, vorticity, energy budgets [5, 8, 12] and water mass transformation in the Southern Ocean [16].

Lee waves are considered to play an important role in the dynamics of the Southern Ocean because they facilitate the transfer of energy from Antarctic Flow jets to micro-scale and turbulent movements of water masses [9]. Diapycnal mixing in the ocean may also be formed by lee waves although it indirectly changes the densities [13, 18]. Diapycnal mixing takes a role in forming ocean stratifications and meridional overturning circulation (MOC) [19-22]. Lee waves may also produce nonlinear water transport [23] and manifest hydraulic jump in oceans [10]. Therefore, it is important to consider lee wave-driven mixing in ocean and climate modelling. Marshall and Speer [19] presented the research employing a model by which includes the evolution of internal lee waves-driven mixing in changing ocean.

Some studies on lee wave phenomena have been conducted by some researchers. Hoosegood et al. [10] observed lee waves by measuring mooring in the region of summits and flanks of two neighbouring seamounts in the tropical Indian. They studied the connection between lee waves and aggregation of silvertip sharks. Trossman et al. [12, 13] analysed the impact of parameterized internal lee wave drags on global ocean general circulation model forced by winds and air-sea buoyancy fluxes. Shakespeare and Hogg [24] developed an internal wave boundary theory, which focused on simulations of steady lee waves, which were generated by big-scale currents flowing under the sea. Moreover, they established a connection among lee waves, viscosity and diffuseness.

Study on lee waves on the main sill of Gibraltar Strait based on measurement from ship-mounted ADCP and multi-probe CTD by using numerical solution of Taylor-Goldstein equation was conducted by del Rosario et al. [14, 15]. Vlasenko et al. [23] studied internal lee waves, which were generated by tidal waves in a Fjords' sea by implementing numerical nonhydrostatic model from laterally averaged Reynolds equations. They considered the effects of stratifications, undersea variables, and cross-section variables. A linear theory about physical conditions of the main sill in the Strait of Gibraltar as the effect of big internal lee waves was also developed by del Rosario and Odriozola [15]. Cusack et al. [9] documented characteristics, energy fluxes, horizontal momentum, and energy dissipation in the Southern Ocean from an observation. Meanwhile, Fortin et al. [22] analysed internal waves in Costa Rica water based on seismic imaging.

Observations on lee waves are difficult to conduct by using standard oceanographical measurement methods because of the limited spatial extent of standing lee waves [22]. Also, the solution of the hyperbolic equation such as the advection equation of lee waves is difficult to resolve by an analytic approximation [25].

Reciprocally, to observe breaking internal waves requires a model with a high spatial resolution. Therefore, an investigation using nonhydrostatic model in simulating lee waves is needed. This model can be applied to resolve breaking internal wave problems. This study aims to observe the lee wave phenomenon, which is resulted from an interaction between stratification and undersea variables. Simulations employ nonhydrostatic model, which was developed by Kämpf [26]. The models were derived from the Navier-Stokes equations with hydrostatic and nonhydrostatic components.

The Navier-Stokes equations are powerful for studying the hydrodynamic behaviour and heat transfer. Yari et al. [27] have applied the Navier-Stokes equation to determine the thermal efficiency of the system.

In our study, the simulations are generated by numerical approach and CFL (Courant-Friedrichs-Lewy) stability parameter is considered in order to analyse its significance in generating lee waves. Moreover, characteristics of lee waves are analysed by generating the Fast Fourier Transform (FFT) from the time series of density waves.

Studies on characteristics of lee waves in stratified fluids are still rarely conducted, especially the ones happening in the ocean. Through this study, mechanisms of lee wave generation in the ocean can be observed. Furthermore, the obtained results may be beneficial for further studies in marine energy.

Marine energy is substantial in energy saving for coastal countries especially nowadays when energy is a vital requirement in sustainable development [28]. Although it requires a relatively large amount of effort, renewable energy can be obtained more from marine energy than from solar energy, which depends on daylight hours [29]**.** Moreover, ocean energy has higher density compared to wind energy, which means that the power produced by the ocean is higher than the one from the wind. The existence of marine energy is rather easy to predict and highly beneficial for regions with limited area.

To date, searching for energy in the ocean such as tidal energy is based on the amplitude of the tidal waves. Site selection for tidal and wind-driven energy in the ocean should consider the amplitudes of the current [30]. Since the current magnitude is influenced by the undersea mountain, the site location of current energy should consider lee waves as well.

Furthermore, on an extension study of lee waves, research on a nanofluid flow such as fluid thermal conductivity and heat transfer [31-33] may consider disturbances like the ones that occur in lee wave dynamics for real-world problems.

This paper is organized as follows: Section 2 introduces the research methods and model description. The results are analysed in Section 3, which includes the simulation results based on two scenarios applied in this research, the significance of CFL in the numerical simulation, and the density changes observed through the resulting FFT. Finally, Section 4 gives a summary of the research.

2. Research Methods and Model Descriptions

2.1. Basic equations

The equation of motion for non-hydrostatic layered fluid developed by Kampf [26] is used to simulate the vertical ocean slice model. Finite difference method is applied to solve the equations and generate simulations. The equations used for the vertical ocean slice read:

$$\frac{\partial u}{\partial t}+u\frac{\partial u}{\partial x}+w\frac{\partial u}{\partial z}=-\frac{1}{\rho_o}\frac{\partial(p+q)}{\partial x} \tag{1}$$

$$\frac{\partial w}{\partial t}+u\frac{\partial w}{\partial x}+w\frac{\partial w}{\partial z}=-\frac{1}{\rho_o}\frac{\partial q}{\partial z} \tag{2}$$

$$\frac{\partial \rho}{\partial t}+u\frac{\partial \rho}{\partial x}+w\frac{\partial \rho}{\partial z}=\frac{\partial}{\partial x}\left(K_h\frac{\partial \rho}{\partial x}\right)+\frac{\partial}{\partial z}\left(K_z\frac{\partial \rho}{\partial z}\right) \tag{3}$$

$$\frac{\partial u}{\partial x}+\frac{\partial w}{\partial z}=0 \tag{4}$$

$$\frac{\partial q}{\partial t}=-\rho_o g\frac{\partial(h<u>)}{\partial x} \tag{5}$$

$$\frac{\partial p}{\partial z} = -\frac{(\rho-\rho_o)}{\rho_o} g \tag{6}$$

Equations (1)-(6) comprise the momentum velocity Eqs. (1) and (2), density Eq. (3), continuity Eq. (4), hydrostatic Eq. (5), and nonhydrostatic pressure field Eq. (6). Equation (1) represents the horizontal momentum velocity (u) while Eq. (2) represents the vertical momentum velocity (v). These equations consist of local and nonlinear terms on the left-hand side and force pressure gradient term on the right-hand side. The hydrostatic (p) and nonhydrostatic pressure field (q) occur in the horizontal momentum while it is only nonhydrostatic pressure field existing in the vertical momentum. The nonhydrostatic pressure field is forced by the sloping sea level and arises from nonhydrostatic effects. The nonhydrostatic pressure field Eq. (6) can be solved in two steps, explicit prediction of the initial pressure and implicit prediction of the pressure correction ($q \rightarrow q^n + \Delta q^{n+1}$). The implicit solution has to be free from divergent condition based on Eq. (4). The momentum velocities and densities can be computed after predicted solutions for the hydrostatic Eq. (5) and nonhydrostatic pressure field Eq. (6) are obtained.

2.2. Two different scenarios

The solution to the basic equations above is applied to two different scenarios. In the first scenario, the domain of the vertical ocean slice model has a length of 500 m and a uniform depth of 100 m (Fig. 1).

In the second scenario, the vertical ocean slice model domain also has a length of 500 m and a depth of 100 m; however, it has an undersea width of 100 m and a height of 40 m (Fig. 2). This undersea mountain forms a cosine function with the midpoint at the position x = 150 m.

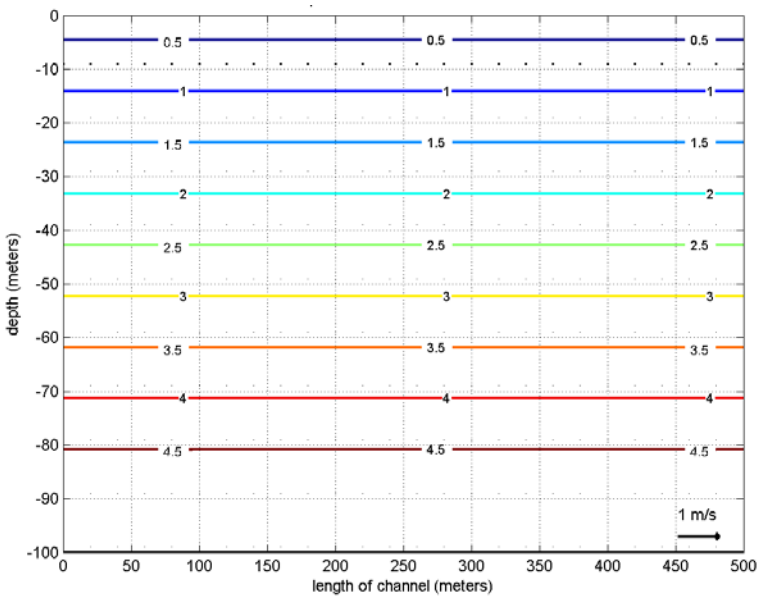

Fig. 1. Initial condition for the first scenario with increasing linear density difference (hereafter density difference is called density).

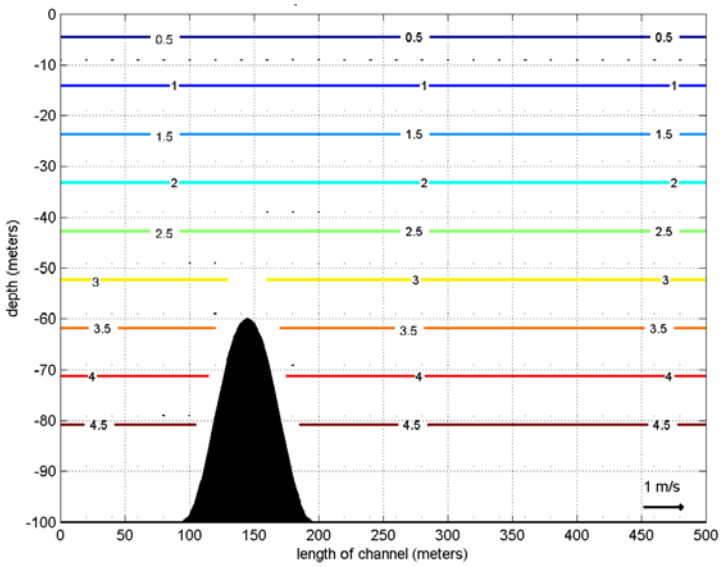

Fig. 2. Initial condition for the second scenario with increasing linear density.

In both scenarios, the model is discretized with Δx = 5 m and Δz = 5 m. The initial condition of scenarios consists of the reference density, ρ_0 = 1028 kg/m^3 and the density value that increases linearly from the surface to the bottom layer based on initial stability frequency ($N^2 = 5 \times 10^{-4} s^{-2}$) with the diffusivity of horizontal and vertical densities are the same ($K_h = K_z = 1 \times 10^{-4}$ m^2/s) (*Appendix A*).

In the open boundary, the model is forced in the form of the sea level gradient (0.5 cm) along the *x*-axis (horizontal). This force propagates to the positive *x*-axis. Because there is an effect of the sea level gradient, Eq. (1) is added with forcing term = $-g\frac{\partial \eta_o}{\partial x}$ in the u-momentum equation. For lateral boundaries, the cyclic boundary conditions are applied [26].

The nonhydrostatic pressure field is calculated by the Successive Over-Relaxation (SOR) method) (*Appendix B*). The pressure accuracy for the SOR iteration is set to 1 x 10^{-3}. The total simulation time is 300 minutes and we save results every 30 seconds. To determine the time step size Δt, which respects to CFL condition, the following formula is applied.

$$\Delta t \leq \frac{\Delta x}{\sqrt{g h_{max}}} \tag{7}$$

For Δx = 5 m, g = 9.81 m/s^2 and h_{max} = 100 m, it is obtained that $\Delta t \leq 0.16$. In order to see the effect of CFL criterion in this numerical experiments, two-time step sizes are chosen, which are Δt = 0.1 second, which is in respect to the CFL condition and Δt =1 second, which is not in respect to the CFL condition.

In the two scenarios, in order to see the changes in densities, the wave analysis is used through generating the density time-series at a certain spatial position. This analysis is only performed for the simulation using Δt = 0.1 second, which is in respect to the CFL condition.

To summarize, the experiments are carried out as follows:

- Setting the topography for the first and second scenarios.
- Implementing the same force for both scenarios.
- Running both topographies by using two choices of time step sizes, Δt = 0.1 second and Δt = 1 second in order to inspect the effect of CFL to the outputs.
- Analysing the significance of CFL by comparing the outputs from simulation using Δt = 0.1 second and Δt = 1 second for each scenario.
- Drawing conclusions from the outputs of the four conditions, which are the first scenario with Δt = 0.1 second and Δt = 1 second, and the second scenario with Δt = 0.1 second and Δt = 1 second.
- Generating FFT for the first and second scenarios with Δt = 0.1 second to analyse the amplitude change in the lee wave dynamics.

3. Results and Discussion

3.1. The first scenario

In the first scenario, the currents move horizontally with the same relative velocities and directions at each layer of density. The value of the density increases with depth.

Figure 3 displays the currents downstream in each density layers for the first scenario where no mountain exists on the seabed. The outputs in the figure were generated by applying Δt = 0.1 second. The figure indicates that the velocities of the currents are uniform in each layer of depth for each simulation time. However, the velocities increase over time. In Fig. 3(a), the currents' uniform velocity starts at a small value. It gradually increases during the simulation time and reaches a velocity greater than 1 m/s after 5 hours (Fig. 3(a) to (d)). In this scenario, the values of the density are the same as the initial model; at each layer, there are no density alterations from the beginning until the end of the simulation.

The simulation employing the value Δt = 1 second generates outputs exhibited in Fig. 4. The outputs in Fig. 4 show a similar event with the ones in Fig. 3. The currents stream down at the same velocity in each layer of depth, but the uniform velocity gradually increases during the observation time. In the meantime, the density values in each layer do not change throughout the recorded time.

However, although Figs. 3 and 4 show alike results, the values of the velocities in Fig. 4 are slightly stronger than the ones in Fig. 3. Figure 5 exhibits the currents' velocity differences, which are not constant over time. As the time runs, the currents' velocity differences assuredly increase, yet the overall currents' velocity differences at each recorded time are very small and no density difference is visible (Figs. 5(a) to (d)).

Until the end of simulation time, the differences of current velocities between the simulation using Δt = 0.1 second and the simulation using Δt = 1 second only reach the value of 0.004 m/s and the direction of the current consistently to the west. Since we use the formula $v_{\Delta t=0.1} - v_{\Delta t = 1}$, where $v_{\Delta t = 0.1}$ is velocity using Δt = 0.1 second and $v_{\Delta t = 1}$ is velocity using Δt = 1 second, it can be stated that the magnitude of current velocities at Δt = 1 second ($v_{\Delta t = 1}$) is bigger than that of current velocities at Δt = 0.1 second ($v_{\Delta t = 0.1}$). While the density values from both simulations are the same.

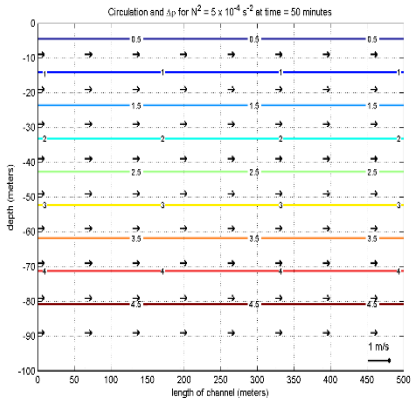

(a) Simulation time *t* = 50 minutes.

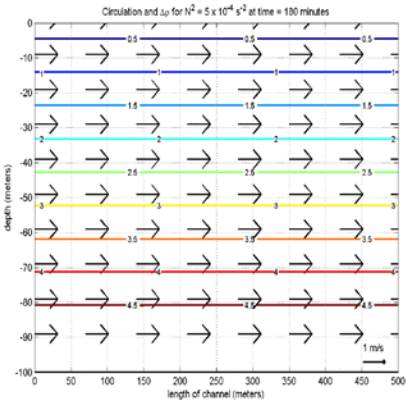

(b) Simulation time *t* = 180 minutes.

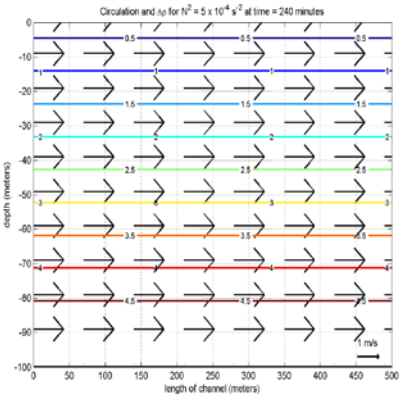

(c) Simulation time *t* = 240 minutes.

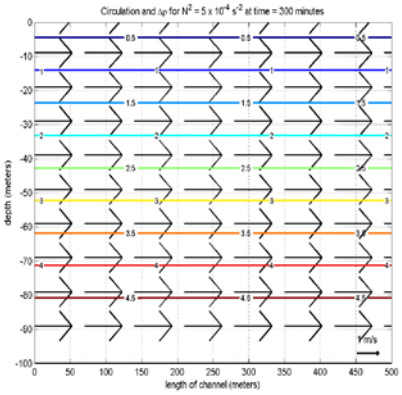

(d) Simulation time *t* = 300 minutes.

Fig. 3. Density and current velocity changes for the first scenario simulation using *Δt* = 0.1 second.

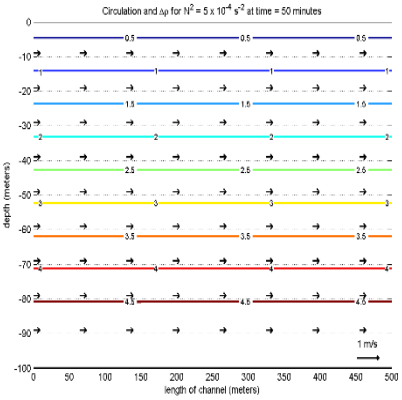

(a) Simulation time *t* = 50 minutes.

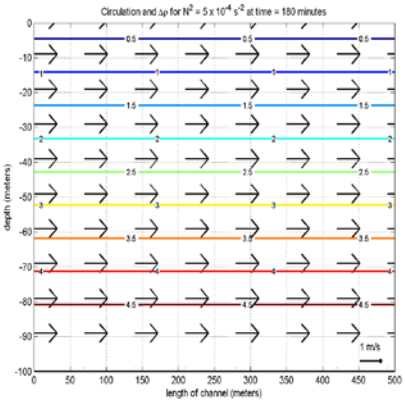

(b) Simulation time *t* = 180 minutes.

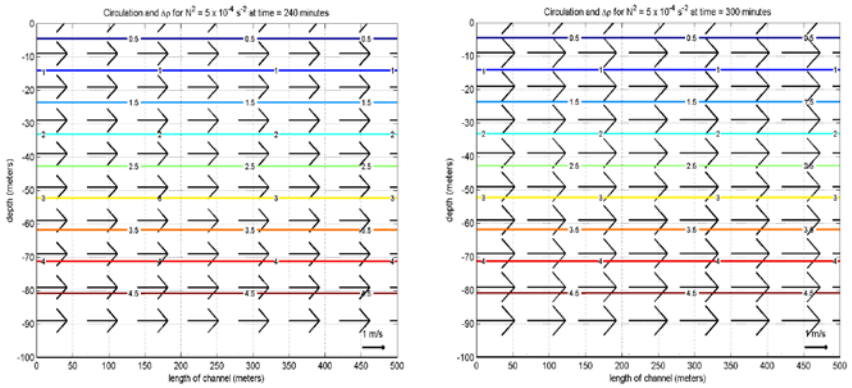

(c) Simulation time t = 240 minutes. **(d) Simulation time t = 300 minutes.**

Fig. 4. Density and current velocity changes for the first scenario simulation using Δt = 1 second.

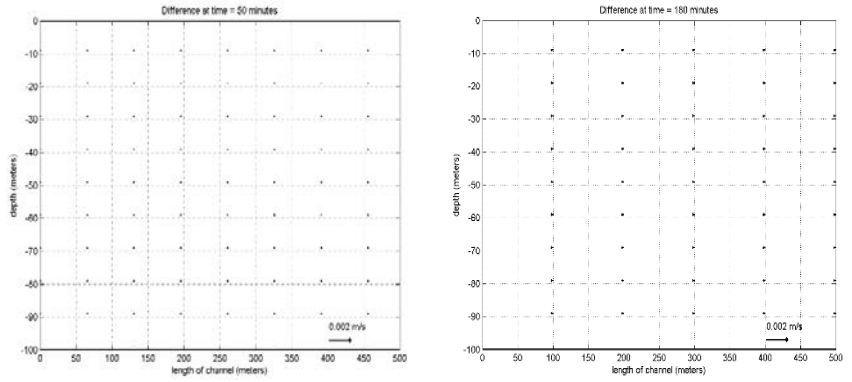

(a) Simulation time t = 50 minutes. **(b) Simulation time t = 180 minutes.**

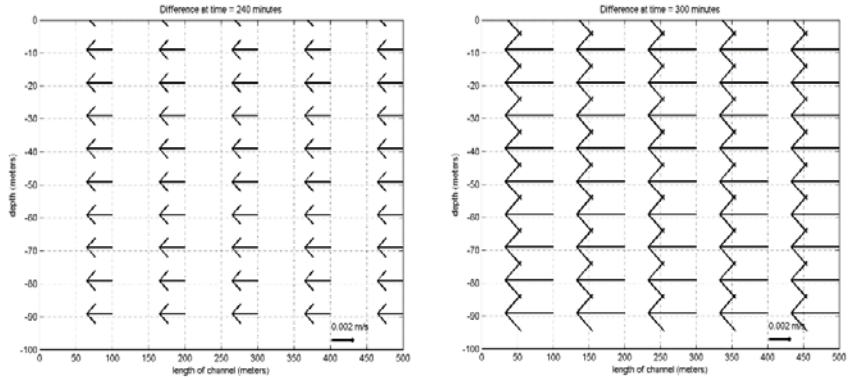

(c) Simulation time t = 240 minutes. **(d) Simulation time t = 300 minutes.**

Fig. 5. Difference of density ($\rho_{\Delta t=0.1} - \rho_{\Delta t=1}$) and current velocity ($v_{\Delta t=0.1} - v_{\Delta t=1}$) from the first scenario simulation using Δt = 0.1 second and Δt = 1 second.

3.2. The second scenario

In the second scenario, density alterations begin to emerge around the peak of the mountain (see Fig. 6). The density alterations were majorly caused by the changing currents of the water when they hit the undersea mountain. The density alterations accumulate and cause more interaction between the densities at each layer. Initially, they propagate downward and then upward towards the surface and the vertical currents intensify on the right side of the mountain.

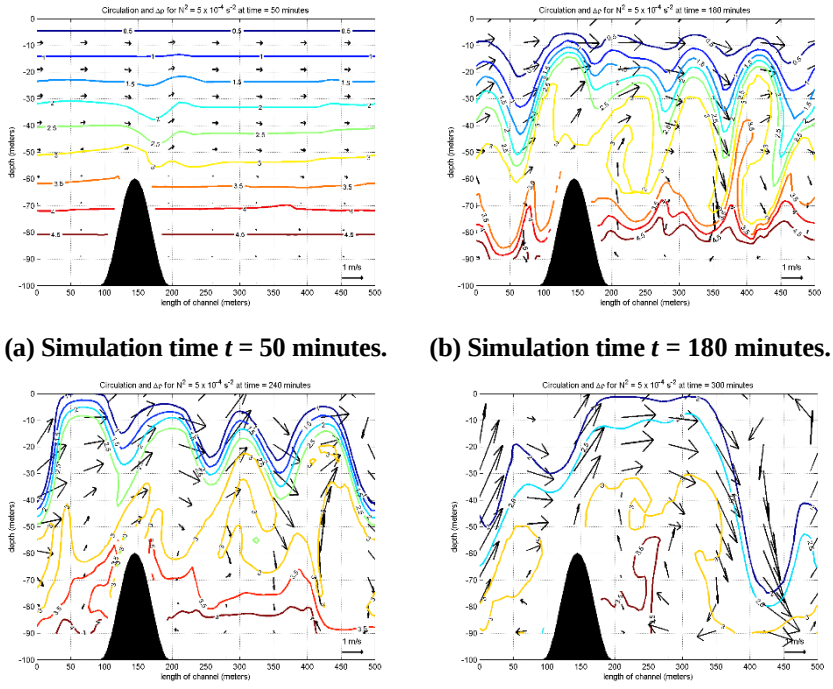

(a) Simulation time t = 50 minutes. **(b) Simulation time t = 180 minutes.**

(c) Simulation time t = 240 minutes. **(d) Simulation time t = 300 minutes.**

Fig. 6. Density and current velocity changes for second scenario simulation using Δt = 0.1 second.

Figure 6 presents the simulations of the second scenario with the value of Δt = 0.1 second, where changes in currents and densities take place. In Fig. 6(a), the densities in every layer of depths start to experience disturbances. In the first hour of observation time, the most significant disturbances seem to happen above the peak of the mountain at the depth of 20 - 60 m under the water surface level, while the densities near the surface level (0 - 20 m) and between the peak of the mountain and the bottom level (60 - 100 m) have not yet been disturbed. The alterations can be clearly detected around the spatial position of x = 150 m up to x = 250 m from the depth of 10 m to 60 m for Δt = 0.1 second. These disturbances may be caused by the changes in the currents' directions, which start to move vertically as they approach the mountain. The mountain turns the currents around its peak upward, which interrupt the densities in the above levels of depth. The currents stream down faster above the peak of the mountain than the ones below the mountain's peak level since the currents above the mountain find no obstacle along with their courses.

After three hours of simulation, the disturbances have risen significantly and majorly disturbed the densities of the water in all layers of the depth, as shown in Fig. 6(b). Figure 6(b) shows that the densities in each layer of depth change in an oscillating fashion. As the simulation time runs, the densities oscillate in wider wavelength and higher amplitude (Figs. 6(b) to (d)). The currents' velocities also increase over time and the directions become steeper, which may cause a higher amplitude in the density waves. In Figs. 6(b) to (d), the currents around the bottom of the water seem to move in the opposite direction from the ones above the mountain peak level. This makes the currents move in a rather circular motion, which may widen the density waves.

Figure 7 presents the change of density layers and currents for the simulation using Δt = 1 second. In the first hour of simulation, the densities experience disturbances when the currents hit the mountain. It can be seen in Fig. 7(a) where the densities start to form layers of waves above the mountain. In this case, the densities seem to receive higher disturbances compared to the result in Fig. 6(a). In Fig. 7(a), the disturbances have reached the surface level. This simulation suggests that as the time increases the densities experience higher disturbances at the depth of below 20 m (Figs. 7(b) to (d)). The currents also move in a rather circular motion at this depth after they pass the mountain. However, the currents do not seem to be as steep as the ones in the simulation using Δt = 1 second, hence, the densities above 20 m do not receive a lot of disturbances and are rather flat instead of forming steep amplitude.

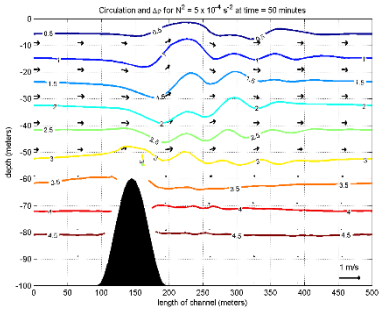

(a) Simulation time t = 50 minutes.

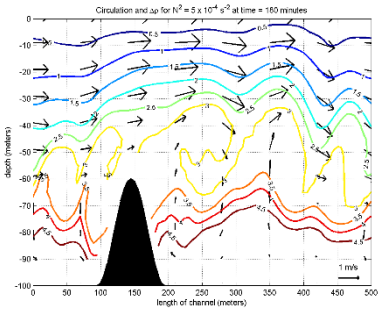

(b) Simulation time t = 180 minutes.

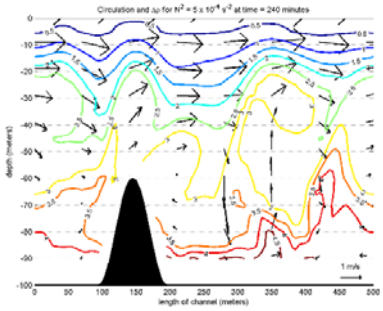

(c) Simulation time t = 240 minutes.

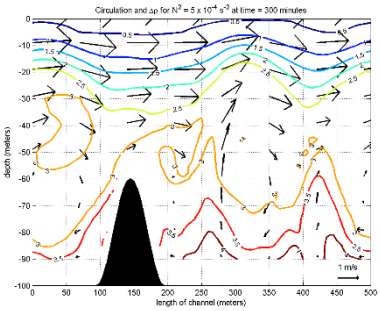

(d) Simulation time t = 300 minutes.

Fig. 7. Density and current velocity changes for the second scenario simulation using Δt = 1 second.

The simulations using Δt = 0.1 second and Δt = 1 second appear to be different in terms of density and current changes. In the first simulation, at the first hour, the densities in the layers of depth near the surface are not yet affected by the disturbance happening in the lower layer, but they start to gradually get affected as the simulation time runs. Meanwhile, in the second simulation, the densities near the surface have been disturbed in the first hour, yet they tend to be unaffected by the density disturbances happening in the lower layers. The former simulation seems to be reasonable since the force at the lateral condition is maintained during the simulation, hence, the force may drive the currents to be higher in velocity as well as steepness. The differences are visualized in Fig. 8. In Fig. 8, it can be observed that even though the current differences in the first hour are very small, they visibly increase during the next simulation time. The figures also signify the density differences (Figs. 8(b) to (d)).

Since we use the formula $\rho_{\Delta t = 0.1} - \rho_{\Delta t = 1}$, where $\rho_{\Delta t = 0.1}$ is the density using Δt = 0.1 second and $\rho_{\Delta t = 1}$ is the density using Δt = 1 second, to produce Fig. 8, $\rho_{\Delta t = 0.1}$ is bigger than $\rho_{\Delta t = 1}$, as reflected from the positive value of the difference. For the velocity difference, we use the formula $v_{\Delta t = 0.1} - v_{\Delta t = 1}$. The resultant of v has two components, i.e., u (east-west) and w (bottom-surface) component. Therefore, if the current moves from the west to the east, it means u component of $v_{\Delta t=0.1}$ is stronger than $v_{\Delta t = 1}$; and if current moves from the bottom to the surface, w component of $v_{\Delta t}$ = 0.1 is bigger than $v_{\Delta t=1}$.

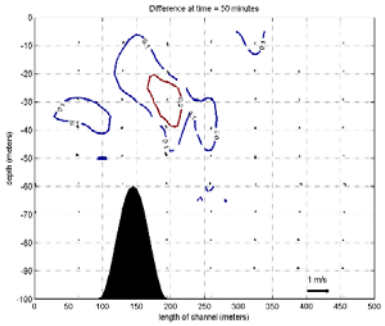

(a) Simulation time t = 50 minutes.

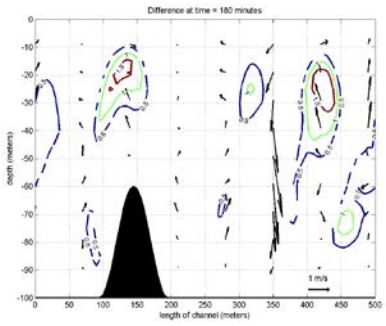

(b) Simulation time t = 180 minutes.

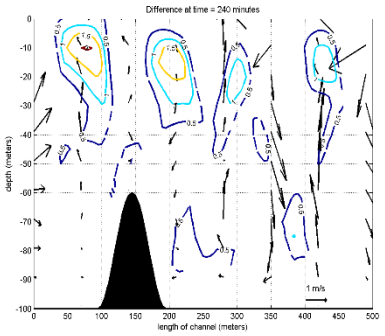

(c) Simulation time t = 240 minutes.

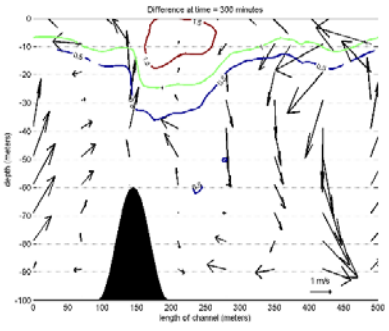

(d) Simulation time t = 300 minutes.

Fig. 8. Difference of density ($\rho_{\Delta t = 0.1} - \rho_{\Delta t = 1}$) and current velocity ($v_{\Delta t = 0.1} - v_{\Delta t = 1}$) from the second scenario simulation using Δt = 0.1 second and Δt = 1 second.

According to Stull [34], there are two formulas to determine the characteristic of lee waves, i.e., Froude Number, *Fr*, which is the ratio natural wavelength (λ) to mountain width (W).

$$Fr = \frac{\lambda}{2W} \tag{8}$$

and natural wavelength reads

$$\lambda = \frac{2\pi M}{N_{BV}} \tag{9}$$

We use oscillation at the Brunt-Vaisala frequency [26], as follows

$$N_{BV}^2 = -\frac{g}{\rho_0}\frac{\partial \rho}{\partial z} \tag{10}$$

In this experiment, the lee waves experience three phases of wave formations according to the Froude number (Fr). These phases can be observed through the change of current waves. The first phase ($Fr << 1$) happens at t = 125 minutes when the wavelength (λ) is smaller than the mountain width (W). The second phase ($Fr \approx 1$) happens at t = 165 minutes when the wavelength is almost the same as the mountain width. Finally the last phase ($Fr >> 1$) happens at t = 240 minutes when the wavelength is greater as the mountain width. These results can be observed in Fig. 9.

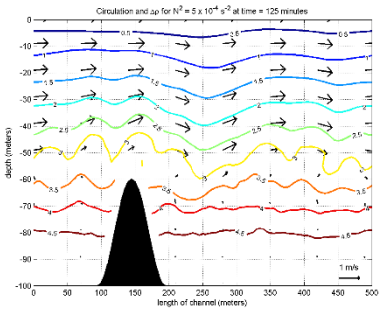

(a) Simulation time t = 125 minutes and $Fr << 1$.

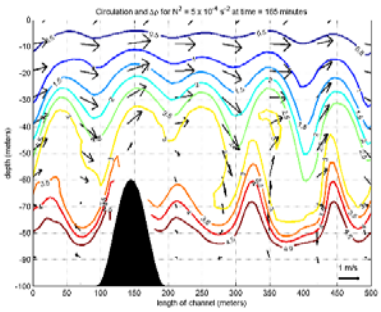

(b) Simulation time t = 165 minutes and $Fr \approx 1$.

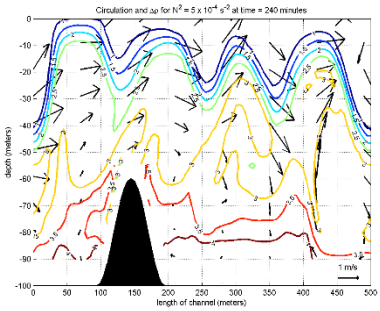

(c) Simulation time t = 240 minutes and $Fr>>1$.

Fig. 9. Comparisons of current wavelengths and mountain width, which affect the value of Fr for the simulation using Δt = 0.1.

These phenomena exist due to the changing values of N_{BV} and λ, which are affected by the continuing lateral force condition during the simulation. In Fig. 10, the value of N_{BV} is not constant over time. Meanwhile, Fig. 11 displays that the value of λ keeps increasing over time. This value changes cause the Froude number (Fr) to keep increasing as shown in Fig. 12. Hence, the wavelength of the wave continues to increase.

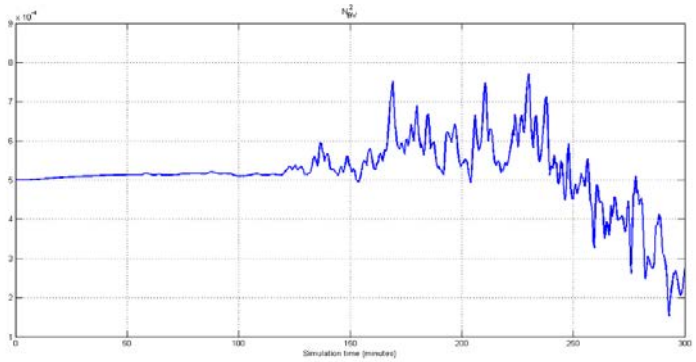

Fig. 10. The value of N_{BV}^2 versus time.

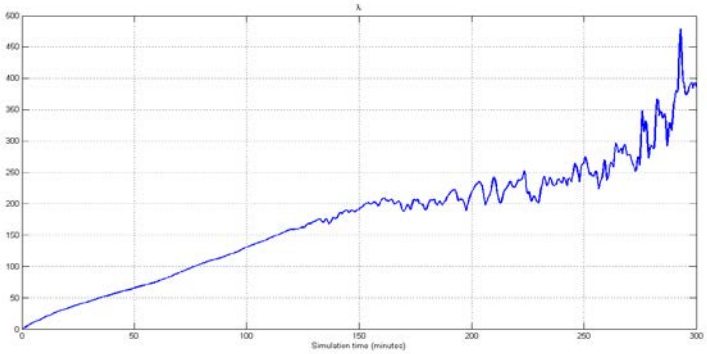

Fig. 11. The value of λ versus time.

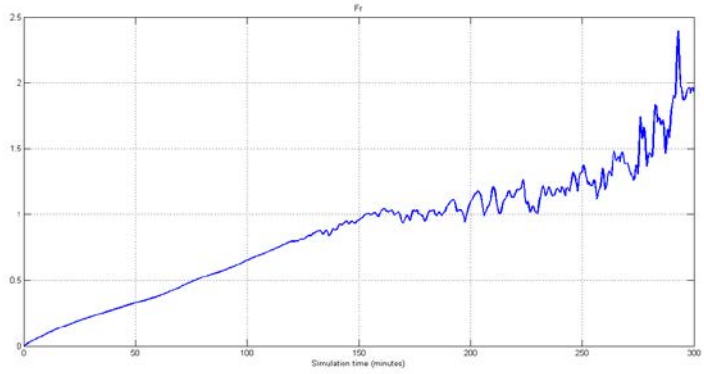

Fig. 12. The value of *Fr* versus time.

3.3. Magnitude of density changes from both scenarios

Figures 13 and 14 present the time-series of the densities at x = 220 m at each depth layer for the first scenario and second scenario respectively. Both time series are extracted from the simulations, which use Δt = 0.1 second and display the values of the densities in the last two hours of the observation, which is from 180 minutes to 360 minutes. For the first scenario, it can be observed in Fig. 13 that at each depth layer, the densities are constant over time and no alteration occurs.

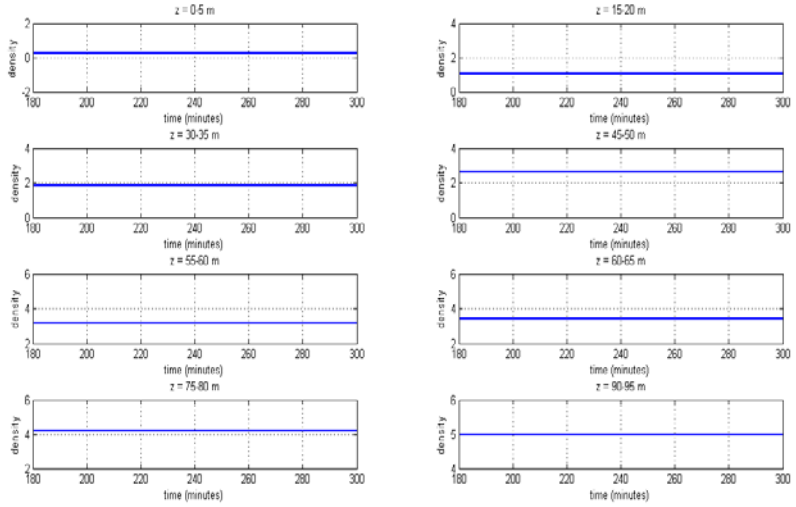

Fig. 13. Time-series of densities at the position of x = 220 m and time t = 180-300 minutes for the first scenario simulation using Δt = 0.1 second.

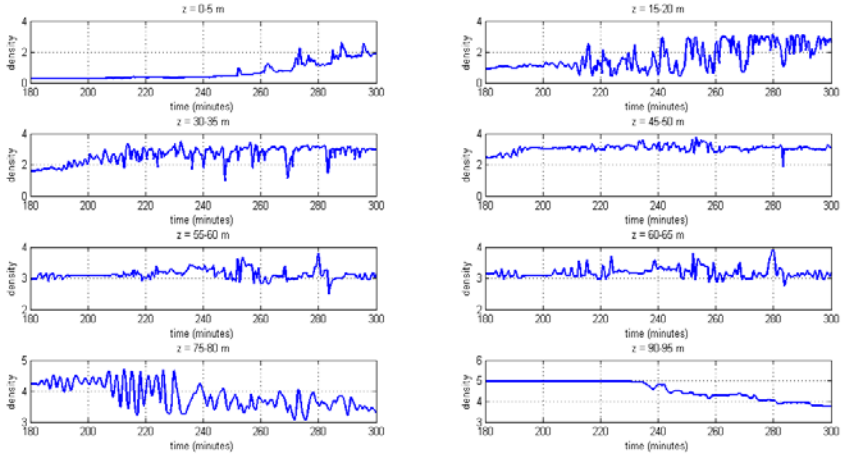

Fig. 14. Time-series of densities at the position of x = 220 m and time t = 180-300 minutes for the second scenario simulation using Δt = 0.1 second.

Figure 14 exhibits the change in density for the second scenario. In the second scenario, the densities fluctuate throughout the observation time. Initially, the density at 0 - 5 m depth does not experience a significant change until the 250th minute, but it fluctuates. The density at the depths of 15-20 m fluctuates more and earlier compared to the layers above; it starts to experience a change at the time of 210 minutes. Meanwhile, the density at the depths of 30-35 m significantly fluctuates after 180 minutes. All densities in these upper three layers tend to increase in magnitudes. At the depth of 45-50 m, 55-60 m, and 60-65 m, changes of the density values also happen, however, they tend to slightly fluctuate around constant values. At 75-80 m depth, there is a significant change in the density magnitude after 180 minutes, however, it seems to fluctuate around the same magnitude until the 230th minute and then fluctuate around the lower magnitude afterwards. Meanwhile, in the depth of 90-95 m, the density magnitude is constant until 230th minute and then starts to decrease afterwards. In overall, changes in density over time experience very large fluctuations at depths above and below the mountain peak, while changes in depth around the mountain peak (55-60 m) fluctuate with relatively smaller magnitudes.

In Figs. 13 and 14, each density can be viewed as a wave. Analysis of each wave is carried out using the Fast Fourier Transform to generate the forming waves. From the results obtained from Figs. 13 and 14, the magnitudes (amplitudes) of the waves on the frequency domain are obtained, and they are presented in Figs. 15 and 16 for the first scenario and for the second scenario, respectively.

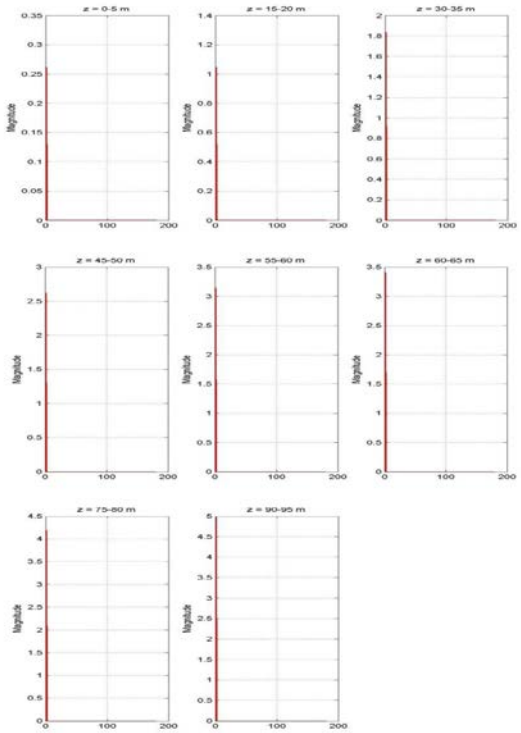

Fig. 15. Plot of density magnitudes versus frequency domain for the first scenario simulation using Δt = 0.1 second.

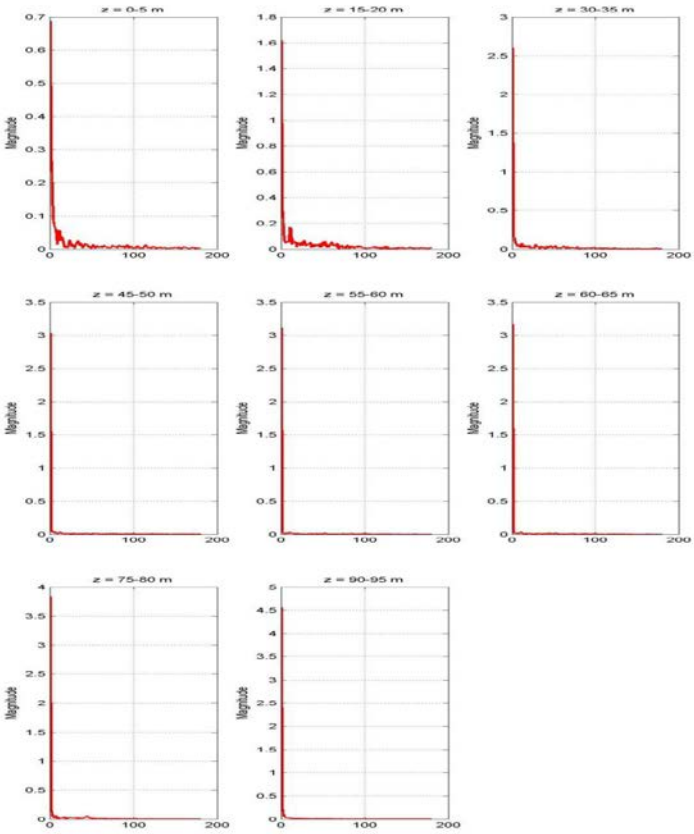

Fig. 16. Plot of density magnitudes versus frequency domain in the second scenario simulation using Δt = 0.1 second.

The spectrum of densities at each depth for the first scenario is presented in Fig. 15. At each depth, each spectrum displays the magnitude of the density at zero frequency because the densities are constant with respect to time.

Figure 16 presents the spectrum of densities for the second scenario. At each depth, the main waves (carrier waves) are disturbed by small magnitude waves creating modulation. The magnitude of modulation waves, which have significant magnitudes are at the upper three layers of depth, i.e., 0-5 m, 15-20 m, 30-35 m.

Table 1 shows the magnitudes of the main waves (carrier waves) at each depth layer for the first and second scenarios, as well as the difference in the magnitude of the carrier waves from both cases. The magnitudes of the carrier waves at four layers of depth above the mountain peak in the second scenario are bigger than the ones in the first scenario, while the magnitudes in the four lower layers in the second scenario is smaller than the ones in the first scenario. The highest magnitude change happens in the depth of 30-35 m, where the magnitude difference between the first and the second scenarios is 0.7673. The second highest change happens in the depth of 15-20 m, the density difference is 0.5714. In the depths of 0-5 m, 45-50 m, and 90-95 m, the changes of the densities are rather equal. Meanwhile, at depths on the mountain peak (depth of 55-60 m), the magnitude of the carrier waves from both scenario shows a very small difference, which is 0.0315.

Table 1. Comparison of carrier wave amplitude values from the density spectra at x = 220 m for both scenario simulations using Δt = 0.1 second.

Z	0-5	15-20	30-35	45-50	55-60	60-65	75-80	90-95
Magnitude of the carrier wave for the first scenario (A_c)	0.2620	1.0479	1.8337	2.6196	3.1436	3.4055	4.1914	4.9773
Magnitude of the carrier wave for the second scenario ($A_{c,sill}$)	0.6884	1.6193	2.6010	3.0341	3.1121	3.1651	3.8390	4.5616
$\lvert A_{c,sill} - A_c \rvert$	0.4265	0.5714	0.7673	0.4144	0.0315	0.2404	0.3524	0.4157

4. Conclusions

The density distribution in the first scenario (vertical ocean slice without an undersea mountain) does not display any alterations for up to five hours of simulation, however, there is a notable increase of the horizontal current. Throughout the simulation time, the density at each layer remains constant. These results happen for the simulations with both choices of time step sizes, 0.1 second and 1 second, and there is no significant difference between the two simulations. CFL criterion does not give any visible effect to the outputs in the scenario without the undersea mountain.

In the second scenario (vertical ocean slice with an undersea mountain), disturbances in the density distribution occur throughout the simulation time. The densities change due to changing the current direction of internal masses of the water when they pass the undersea mountain. The currents start to move vertically when they hit the mountain and disturb the layers of the densities above the mountain. The disturbances are accumulated and cause the incoming currents to steepen and changing their directions, which cause circular motions. This event gives rise to density waves, which steepen in height and widen in length. The results in the second scenario happen for the simulations with both choices of time step sizes, 0.1 second and 1 second. However, both simulation show different outputs regarding current velocities, density changes, and density waveforms due to time step value. Therefore, for the scenario with undersea mountain, the numerical simulation must respect to the CFL criterion.

Based on the Froude Number, lee waves simulated in this experiment experience three types of waves characteristics, which happen gradually one after another. For the simulation of the second scenario with time step 0.1 second, the wavelength is smaller than the mountain width at 125 minutes of the simulation runtime. At 165 minutes, the wavelength becomes the same as the mountain width. Finally, at 240 minutes, the wavelength becomes greater as the mountain width and it continues to get bigger.

The magnitudes of the carrier waves of the densities above the mountain peak in the second scenario are bigger than the ones in the first scenario. Meanwhile, the densities below the mountain peak in the second scenario are smaller than the ones in the first scenario. In addition, the magnitude of density at depths around the top of the mountain only experiences very small change.

The results of the two scenarios (with and without mountain) suggest that the choices of the time step sizes do not really give a significant difference in the results of the first scenario simulation, however, they do in the second scenario. The time

step size 0.1 second is set according to CFL and gives more reasonable and stable simulation results, especially in the second scenario.

Acknowledgements

This research is funded by Universitas Syiah Kuala, Banda Aceh, Ministry of Research and Technology, Indonesia, under the scheme of Professor research. The contract numbers are 1442/UN11/SP/PNBP/2017. This research was conducted at the Laboratory of Ocean Modelling.

Nomenclatures

Fr	Froude number
g	Acceleration of gravity, m/s^2
H	Depth of water or an undisturbed sea level, m
K_h, K_z	Diffusivity of horizontal and vertical densities, m^2/s
N^2	Initial Brunt-Väisälä frequency, s^{-1}
N_{BV}^2	Brunt-Väisälä frequency from the simulation, s^{-1}
p	Dynamic pressure, kg/ms^2
q	The nonhydrostatic pressure field, kg/ms^2
q_s	The nonhydrostatic pressure field at surface, kg/ms^2
u	Horizontal velocity, m/s
W	Mountain width, m
w	Vertical velocity, m/s

Greek Symbols

Δt	Time-step, s
Δx, Δz	Distance spacing in horizontal and vertical, respectively, m
λ	Natural wavelength, m
ρ	Depth-variable part of density, kg/m^3
ρ_0	Constant reference density at the surface, kg/m^3

References

1. Tokgozlu, A.; Rasulov, M.; and Aslan, Z. (2005). Modelling and classification of mountain waves. *Technical Soaring*, 29(1), 22-30.
2. Holton, J.R.; Curry, J.A.; and Pyle, J.A. (2003). *Encyclopedia of atmospheric sciences*. Cambridge, Massachusetts, United States of America: Academic Press.
3. Klymak, J.M.; Legg, S.; Alford, M.H.; Buijsman, M.; Pinkel, R.; and Nash, J.D. (2012). The direct breaking of internal waves at steep topography. *Oceanography*, 25(2), 150-159.
4. Makarenko, N.; Maltseva, J; and Cherevko, A. (2015). Structures of lee waves over combined topography. *AIP Conference Proceedings*, 1685, 090005.
5. Trossman, D.S.; Waterman, S.; Polzin, K.L.; Arbic, B.K.; Garner, S.T.; Naveira-Garabato, A.C.N.; and Sheen, K.L. (2015). Internal lee wave closures: Parameter sensitivity and comparison to observations. *JGR Oceans*, 120(12), 7997-8019.

6. Wright, C.J.; Scott, R.B.; Ailliot, P.; and Furnival, D. (2014). Lee wave generation rates in the deep ocean. *Geophysical Research Letters*, 41(7), 2434-2440.
7. Saenko, O.A.; Zhai, X.; Merryfield, W.J.; and Lee, W.G. (2012). The combined effect of tidally and eddy-driven diapycnal mixing on the large-scale ocean circulation. *Journal of Physical Oceanography*, 42(4), 526-538.
8. Garabato, A.C.N.; Nurser, A.J.G.; Scott, R.B.; and Goff, J.A. (2013). The impact of small-scale topography on the dynamical balance of the ocean. *Journal of Physical Oceanography*, 43(3), 647-668.
9. Cusack, J. M.; Garabato, A.C.N.; Smeed, D.A.; Girton. J.B. (2017). Observation of a large lee wave in the drake passage. *Journal of Physical Oceanography*, 47(4), 793-810.
10. Hosegood, P.J.; Nimmo-Smith, W.A.M.; Proud, R.; Adams, K.; and Brierley, A.S. (2019). Internal lee waves and baroclinic bores over a tropical seamount shark 'hotspot'. *Progress in Oceanography*, 172, 34-50.
11. Nikurashin, M.; Vallis, G.K.; and Adcroft, A. (2013). Routes to energy dissipation for geostrophic flows in the Southern Ocean. *Nature Geoscience*, 6(1), 48-51.
12. Trossman, D.S.; Arbic, B.K.; Garner, S.T.; Goff, J.A.; Jayne, S.R.; Metzger, E.J. and Wallcraft, A.J. (2013). Impact of parameterized lee wave drag on the energy budget of an eddying global ocean model. *Ocean Modelling*, 72, 119-142.
13. Trossman, D.S.; Arbic, B.K.; Richman, J.G.; Garner, S.T.; Jayne, S.R.; and Wallcraft, A.J. (2016). Impact of topographic internal lee wave drag on an eddying global ocean model. *Ocean Modelling*, 97, 109-128.
14. del Rosario, J.J.A.; Mejías, M.B.; and Vázquez-Lòpez-Escobar, A. (2003). The influence of tidal hydrodynamic conditions on the generation of lee waves at the main sill of the Strait of Gibraltar. *Deep-Sea Research Part I: Oceanographic Research Papers*, 50(8), 1005-1021.
15. del Rosario, J.J.A.; and Odriozola, E.A. (2005). A high order linear model for the prediction of internal lee waves at the main sill of the Strait of Gibraltar. *Journal of Marine Systems*, 53(1-4), 197-216.
16. Nikurashin, M.; and Ferrari, R. (2011). Global energy conversion rate from geostrophic flows into internal lee waves in the deep ocean. *Geophysical Research Letters*, 38, 6 pages.
17. Scott, R.B.; Goff, J.A.; Naveira-Garabato, A.C.; and Nurser, A.J.G. (2011). Global rate and spectral characteristics of internal gravity wave generation by geostrophic flow over topography. *Journal of Geophysical Research*, Oceans, 116(C9), 14 pages.
18. Rizal, S.; Iskandar, T.; Muhammad; Haditiar, Y.; Ilhamsyah, Y.; Setiawan, I.; and Sofyan, H. (2019). Numerical study of the internal wave behaviour in the vertical ocean slice model. *Journal of Engineering Science and Technology* (*JESTEC*), 14(5), 2836-2846.
19. Marshall, J.; and Speer, K. (2012). Closure of the meridional overturning circulation through Southern Ocean upwelling. *Nature Geoscience*, 5(3), 171-180.

20. Talley, L.D. (2013). Closure of the global overturning circulation through the Indian, Pacific, and Southern Oceans: Schematics and transports. *Oceanography*, 26(1), 80-97.
21. Melet, A.; Hallberg, R; Legg, S; and Nikurashin, M. (2014). Sensitivity of the ocean state to lee wave-driven mixing. *Journal of Physical Oceanography*, 44(3), 900-921.
22. Fortin, W.F.J.; Holbrook, W.S.; and Schmitt, R.W. (2016). Mapping turbulent diffusivity associated with oceanic internal lee waves offshore Costa Rica. *Ocean Science Discussions*, 12(4), 601-612.
23. Vlasenko, V.; Stashchuk, N.; and Hutter, K. (2002). Water exchange in fjords induced by tidally generated internal lee waves. *Dynamics of Atmospheres and Oceans*, 35(1), 63-89.
24. Shakespeare, C.J.; and Hogg, A.M. (2017). The viscous lee wave problem and its implications for ocean modelling. *Ocean Modelling*, 113, 22-29.
25. Bahrami, A.; Hosseinzadeh, S.; Ghasemiasl, R.; and Radmanesh, M. 2015. Solution of non-fourier temperature field in a hollow sphere under harmonic boundary condition. *Applied Mechanics and Materials*, 772(197), 197-203.
26. Kämpf, J. (2010). *Advanced ocean modelling: Using open-source software*. Berlin, Germany: Springer Science + Business Media.
27. Yari, A; Hosseinzadeh, S; Golneshan, A.A.; and Ghasemiasl, R. (2015). Numerical simulation for thermal design of a gas water heater with turbulent combined convection. *Proceedings of the ASME-JSME-KSME Joint Fluids Engineering Conference.* Seoul, Korea, 12 pages
28. Hoseinzadeh, S.; Zakeri, M.H.; Shirkhani, A.; Chamkha. A.J. (2019). Analysis of energy consumption improvements of a zero-energy building in a humid mountainous area. *Journal of Renewable and Sustainable Energy*, 11(1), 015103.
29. Hoseinzadeh, S.; and Azadi, R. (2017). Simulation and optimization of a solar-assisted heating and cooling system for a house in Northern of Iran. *Journal of Renewable and Sustainable Energy*, 9(4), 045101.
30. Sakmani, A.S.; Lam, W.-H.; Hashim, R.; and Chong, H.-Y. (2013). Site selection fortidal turbine installation in the Strait of Malacca. *Renewable and Sustainable Energy Reviews*, 21, 590-602.
31. Ahmed, N.; Shah, N.A.; Ahmad, B.; Shah, S.I.; Ulhaq, S.; and Rahimi-Gorji, M. (2019). Transient MHD convective flow of fractional nanofluid between vertical plates. *Journal of Applied and Computational Mechanics*, 5(4), 592-602.
32. Hussanan, A.; Khan, I.; Gorji, M.R.; and Khan, W.A. (2019). CNTS-water-based nanofluid over a stretching sheet. *Bio Nanoscience*, 9(3), 21-29.
33. Krishna, C.M.; Viswanatha Reddy, G.; Souayeh, B.; Raju, C.S.K.; Rahimi-Gorji, M.; and Raju, S.S.K. (2019). Thermal convection of MHD Blasius and Sakiadis flow with thermal convective conditions and variable properties. *Microsystem Technologies*, 25, 3735-3746.
34. Stull, R.B. (2007). *Meteorology for scientists and engineers* (2nd ed.). California, United States of America: Cengage Learning, Inc.

Appendix A

Pseudocode and Algorithm

A.1. Initialization

Pseudocode below describes the initialization of the variables in the program:

```
nx = 101                {horizontal dimension}
nz = 21                 {vertical dimension}
G = 9.81                {acceleration due to gravity}
RHOREF = 1028.0         {reference density}
nt = 5*60*60            {runtime parameters}
dx = 5.0
dz = 5.0
dt = 0.1
kh = 1.e-4
kz = 1.e-4
N2 = 5e-4               {stability frequency squared}

{set initial arrays}
FOR i = 0 TO nz+10 DO
    FOR k = 0 TO nx+1 DO
        p(i,k) = 0.0
        q(i,k) = 0.0
        rho(i,k) = RHOREF
        u(i,k) = 0.0
        w(i,k) = 0.0
    END
END

{ambient density stratification}
FOR k = 0 TO nx+1
    FOR i = 0 TO nz+1
        IF i == 0 THEN
            rho(i,k) = RHOREF
        ELSE
            rho(i,k) = rho(i-1)+N2*RHOREF/g*dz
        END
    END DO
END DO

{idealised bathymetry}
FOR k = 1 TO nx DO
    depth(k) = 100
END DO
FOR k = 21 TO 40 DO
    depth(k) = depth(k)-20*(1-COS((k-20)/20*2*PI))
END DO

{ambient forcing}
force = dt*g*0.005/nx/dx

{lateral boundary conditions - cyclic boundary conditions}
q(0,0) = q(0,nx)
q(0,nx+1) = q(0,1)
FOR i = 1 TO nz DO
    u(i,0) = u(i,nx)
    u(i,nx+1) = u(i,1)
    w(i,0) = w(i,nx)
    w(i,nx+1) = w(i,1)
    q(i,0) = q(i,nx)
    q(i,nx+1) = q(i,1)
END DO
```

Appendix B

B.2. Algorithm of the S.O.R. Method

The following steps present the algorithm of S.O.R. method implemented in this research:

a. Time iteration, for n = 1 to nt = 5*60*60 (runtime parameters)
b. $u^n, w^n, q^n \rightarrow u^*, w^*, q^*$
c. $\Delta q^n \rightarrow \Delta q^{r=0}$
d. S.O.R. iteration
e. $\Delta q^r \rightarrow \Delta q^{r+1}$
f. $\Delta q^{r+1} \rightarrow u^{r+1}, w^{r+1}$
g. $u^{r+1} \rightarrow \Delta q_s^{r+1}$
h. If $|\Delta q^{r+1} - \Delta q^r| < \varepsilon$ then u^{r+1}, w^{r+1}, $\Delta q^{r+1} \rightarrow u^{n+1}$, w^{n+1}, q^{n+1} and $n + 1 \rightarrow n$, repeat all steps. If this condition is not satisfied, then $r + 1 \rightarrow r$, repeat steps d-h.